KuROS: A New Airborne Ku-Band Doppler Radar for Observation of Surfaces

GÉRARD CAUDAL, DANIÈLE HAUSER, RENÉ VALENTIN, AND CHRISTOPHE LE GAC

Université de Versailles Saint-Quentin-en-Yvelines, Versailles, and Universite Paris 06, Paris, and CNRS/INSU, LATMOS-IPSL, Guyancourt, France

ABSTRACT

This study presents the new airborne Doppler radar Ku-Band Radar for Observation of Surfaces (KuROS), which provides measurements of the normalized radar cross section $\sigma°$ and of the Doppler velocity over the sea. The system includes two antennas rotating around a vertical axis, although only the results from the lower incidence (14°) antenna are presented here. Also given are the first results from observations performed during two field campaigns held in 2013: the Hydrological Cycle in Mediterranean Experiment (HyMeX) and the Prévision Océanique, Turbidité, Ecoulements, Vagues et Sédimentologie (PROTEVS).

Sea wave directional spectra computed by the radar from tilt modulation of $\sigma°$ are consistent with those given by the directional wave rider moored in the Mediterranean basin, both in terms of significant wave height H_s and main features of the wavenumber spectrum. As concerns the azimuthal distribution, two methods are tested to remove the 180° ambiguity of the radar-derived directional spectrum. The first method is based on the correlation between the modulations of $\sigma°$ and Doppler velocity, which reflects the correlation between the sea surface slope and orbital velocity. The second method does not use the Doppler velocity but computes the cross spectrum between the modulations of $\sigma°$ between two power profiles separated by some time lag ΔT, from which the phase velocity of sea waves is deduced. Comparing the sea wave directional spectra disambiguated by both methods, with the directional spectrum given by the wave rider, it is concluded that the first method (using Doppler velocity) is more efficient to remove the 180° ambiguity and should be preferred to the second method.

1. Introduction

Sea-state knowledge is essential for both operational needs (marine meteorology, navigation, offshore and coastal activities, . . .) and for research needs (better knowledge of hydrodynamics of the waves, interactions between waves and the atmospheric and oceanic boundary layers, coupling of the atmosphere and ocean systems from regional to climatologic scales, interactions between electromagnetic signals and the ocean surface). Although the performance of wave models has significantly improved in the last decades (Cavaleri et al. 2007), improvements are still needed, in particular for high sea-state conditions, extreme events (hurricanes, typhoons), rapidly evolving storms, and for providing accurate prediction not only in terms of wave height but also in terms of peak wavelength and direction (important for swell).

Furthermore, numerical models that are presently used to predict the distribution of energy of the ocean surface waves as a function of frequency (or wavenumber) and direction still suffer from various shortcomings (see Cavaleri 2006), among which uncertainties in the parameterization of source and sink terms (dissipation processes, source and sink terms related to turbulent exchanges at the interface), and errors on the prescribed initial state. In addition, because of the limitation in the model discretizations, significant errors in the directional distribution of wave energy may happen in open sea conditions, and this may induce large errors on description of wave evolution when they approach the coasts.

Up to now, the only radar system implemented on spacecraft for measuring ocean wave spectra is the synthetic aperture radar (SAR). Since the pioneering work performed with the SAR mounted on board the *Seasat* satellite (Gonzalez et al. 1979), it appeared, however, that the SAR systems are expensive to develop and not trivial to use for the estimation of ocean wave directional spectra. In that context, several airborne

Corresponding author address: Gérard Caudal, LATMOS-IPSL, Université de Versailles Saint-Quentin-en-Yvelines, 11 Boulevard d'Alembert, 78280 Guyancourt CEDEX, France.
E-mail: gerard.caudal@latmos.ipsl.fr

radars operating without the constraints of SAR have been developed: the Ka-band surface contour radar (SCR) developed by Walsh et al. (1985), the Ku-band Radar Ocean Wave Spectrometer (ROWS) developed by Jackson et al. (1985a,b), the C-band system Radar pour l'Etude du Spectre des Surfaces par Analyse Circulaire (RESSAC; Hauser et al. 1992), the C-band polarimetric Système de Télédétection pour l'Observation par Radar de la Mer (STORM; Hauser et al. 2003), and more recently the X-band coherent real aperture radar (CORAR) system developed by Plant et al. (2005). Such airborne measurements provide directional information with more details than directional buoys (Pettersson et al. 2003).

The China–France Oceanography Satellite (CFOSAT) is a new satellite mission under preparation by the Chinese and French space agencies. It is devoted to the radar observation of directional sea wave spectra and surface winds over the ocean. It will include on the same platform a Ku-band scatterometer (SCAT) for measuring surface winds, developed by the Chinese partner, and a real-aperture Ku-band radar spectrometer [Surface Waves Investigation and Monitoring (SWIM)] for measuring sea waves, developed in France under the support of the Centre National d'Etudes Spatiales (CNES) (Hauser et al. 2010). CFOSAT will be a polar-orbiting satellite at about 520-km altitude. The SWIM instrument will illuminate the surface sequentially with six incidence angles: $0°$, $2°$, $4°$, $6°$, $8°$, and $10°$ with an antenna aperture of approximately $2°$. To avoid limitations encountered by the SAR systems, the SWIM instrument will use a real-aperture observation technique. But, in order to acquire data in all azimuth orientations, the antenna will be rotating, at a speed rate of 5.6 rpm. The following geophysical parameters will be provided from the SWIM observations: normalized radar cross-section profiles from $0°$ to $10°$ incidence (combining all beams); significant wave height and wind speed from the nadir beam, similar to conventional radar altimeter; and directional ocean wave spectra from the combination of the $6°$, $8°$, $10°$ beams. Details may be found in Hauser et al. (2010).

In the context of the preparation of the CFOSAT space mission, we developed a new airborne radar, called Ku-Band Radar for Observation of Surfaces (KuROS). The primary aim of KuROS is to optimize the choices made for the implementation of the CFOSAT satellite, and to serve as a tool for the geophysical validation of the CFOSAT sea wave measurements once launched. Another important objective of the KuROS radar is to explore the characteristics of the kinematics of the sea surface. For this purpose, in addition to measuring the normalized radar cross section $\sigma°$, KuROS has the ability to measure the Doppler velocity of the radar echo, by means of the pulse-pair technique as described in

section 2. Such a Doppler measurement capability was already included in CORAR, developed by Plant et al. (2005), who were able to deduce directional wave spectra from images of surface velocity. However, those were obtained only in the side-looking mode. Here, we use both $\sigma°$ and Doppler signals simultaneously in the rotating mode at low incidence (around $14°$), and we will show that the Doppler information can be used efficiently to remove the $180°$ ambiguity from the calibrated directional wave spectrum retrieved from the $\sigma°$ tilt modulation.

To address the question of measuring both wind and waves, the KuROS radar system includes two antennas, one probing a range of incidence angles around $14°$ to measure waves [called the low incidence (LI) antenna] and another antenna probing incidence angles around $40°$ to measure wind [medium incidence (MI) antenna]. Both antennas have been tested in an anechoic chamber to determine their radiation patterns. However, when integrated within the body of the aircraft, it turned out that the antenna radiation pattern of the MI antenna obtained from calibration flights over corner reflectors (see section 4 below) did not reproduce the shape of the main lobe pattern expected from anechoic chamber measurements. This is attributed to the presence of a metal collar used to adjust the antenna system within the body of the plane, as will be discussed in section 2. For this reason, the results presented here will be focused on the observations performed with the LI antenna. The field campaigns in which KuROS has been involved will be described in section 3. The results of in-flight calibration of the radar will be briefly reported in section 4, and the first scientific results obtained from the analysis of radar cross section and Doppler velocity will be given in section 5. In particular, two new methods to remove the $180°$ ambiguity of the measurements of the directional sea wave spectrum will be presented and compared.

2. Description of the instrument

a. General characteristics

The main characteristics of the radar system are given in Table 1. The relatively large antenna beamwidth is required to estimate ocean wave spectra from a real-aperture radar at small incidence (see Hauser et al. 1992; Jackson et al. 1985a). In addition, a Doppler measurement capability has been designed for KuROS. The whole system is mounted in an ATR42 aircraft, operated by the Service des Avions Français Instrumentés pour la Recherche en Environnement (SAFIRE), and the conditions of use of KuROS are specified to allow measurements from flights from about 500 to about 3000 m above the surface.

TABLE 1. Major parameters of the KuROS radar.

Parameter	Value
Frequency	13.5 GHz
Transmitted power	11 W
LI antenna	14° boresight incidence angle; gain = 18.5 dB
	18.5° elevation by 8.6° azimuth one-way beamwidth; HH polar
MI antenna	40° boresight incidence angle
	21° elevation by 8° azimuth beamwidth; gain = 17.5 dB; HH polar
	17° elevation by 8° azimuth beamwidth; gain = 18 dB; VV polar
SNR (one pulse)	LI antenna: 11.3 dB; MI antenna: −5.4 dB
Antenna rotation speed	2.4–4.6 rpm; tunable
Aircraft speed	90–110 m s^{-1}

The block diagram of the instrument is shown in Fig. 1. The overall system is composed of an antenna and radome unit (ARU), a power supply unit (PSU), a radio frequency unit (RFU), a digital processing unit (DPU), and a human interface machine (HIM), and the whole system is controlled by a management and control unit (MCU). Both functions of DPU and MCU are entirely performed by a field-programmable gate array (FPGA) device. A more detailed description of ARU, RFU, and DPU will be briefly given below.

b. Antenna and radome unit

Because of the large range of incidences to be covered, and in order to keep a cost-effective system, two antennas are necessary. We chose a system of two printed antenna arrays, the LI antenna, pointed to 14° incidence with respect to nadir; and the MI antenna, pointed to 40° incidence with respect to nadir (see Fig. 2). The LI antenna operates in the horizontal-transmit horizontal-receive (HH) polarization, and we choose a dual-linear (HH/VV) capability [alternately HH and vertical-transmit vertical-receive (VV)] for the MI antenna to offer comparisons with the CFOSAT-SCAT measurements. This set of two antennas is mounted inside the airplane. The antenna beam points through a 40-mm-thickness quartz window that serves as an interface between the outside and inside of the airplane at its lower part, allowing the whole radar system, including the antennas, to be under cabin pressure. Both antennas are used here through their real aperture, without any synthetic aperture processing. The antenna system can be controlled either to rotate over 360° around the vertical axis at a chosen rotation velocity or to stop at a fixed azimuth angle. The rotation velocity and the flight altitude are determined in order to have an overlap of the ground footprints and to measure a wave spectrum of a few-hundred-meter wavelength. An example of the antenna footprint is shown in Fig. 3. For the sake of legibility, in Fig. 3 the footprint is shown every 300 ms. However, the real-time integration is performed over 1 ms, yielding a displacement of the order of 0.1% of the footprint between successive records.

c. Radio-frequency unit

The transmitted wave is a pulsed chirp whose bandwidth is centered around 13.5 GHz. Because of the large range of distances to be sampled (flight altitudes from 500 to 3500 m, incidences from 0° to 50°), we have defined several chronograms of transmitted pulses,
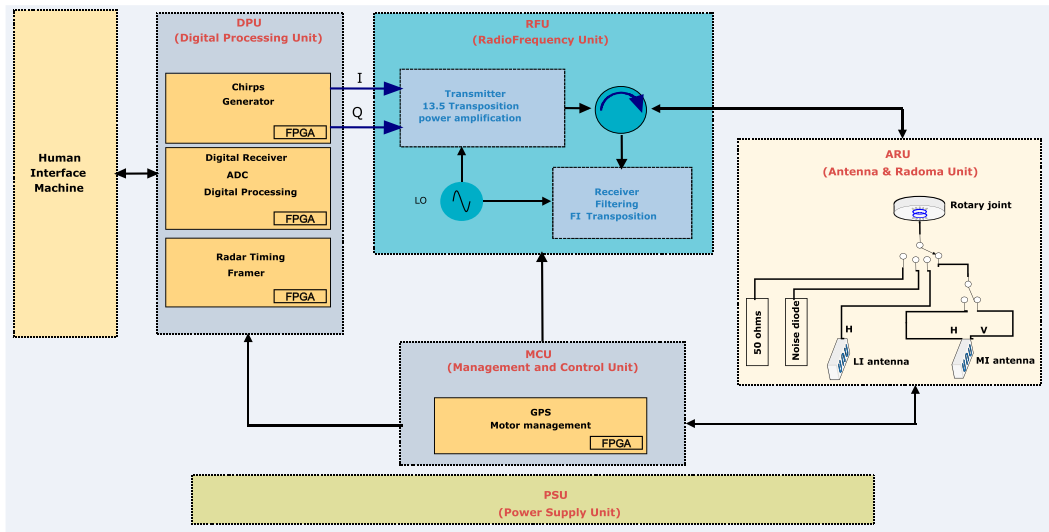

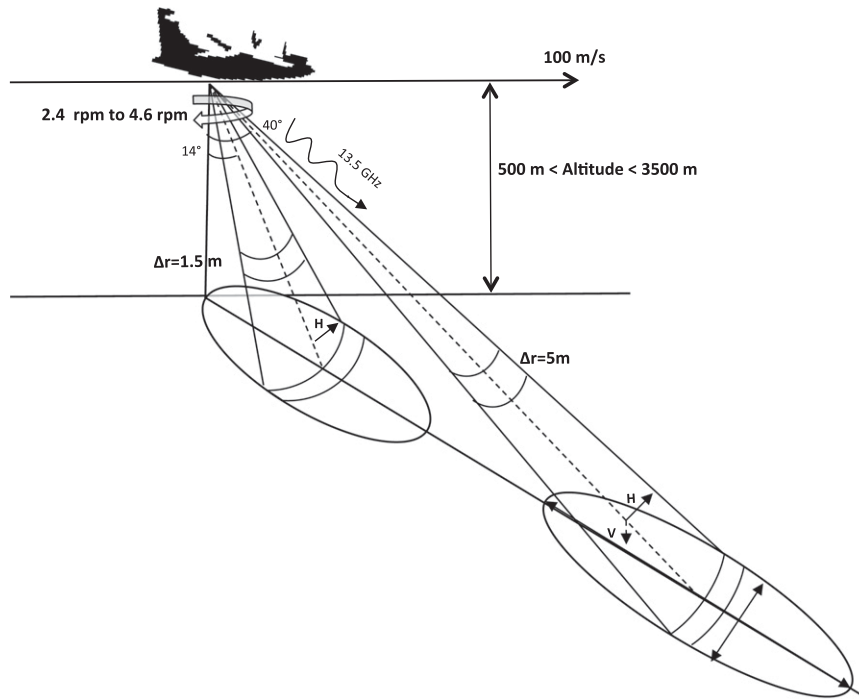
FIG. 1. Block diagram of the KuROS instrument.

FIG. 2. Geometry of observation, showing the footprints of both LI and MI antennas.

adapted to the flight altitude and the antenna. Table 2 presents these different modes, while Fig. 4 illustrates the time–frequency diagrams of the transmitted pulses. The frequency range ($F_{e\min} - F_{e\max}$) of the transmitted chirp has been chosen in order to achieve a high range resolution: (25–125 MHz) for the LI antenna and (30–60 MHz) for the MI antenna, corresponding to a range resolution of 1.5 and 5 m, respectively.

Within the DPU, two chirps in phase quadrature are generated at an intermediate frequency (IF) with the frequency range as given in Table 2. A Tukey window is applied to these two signals before transmission. In RFU, this complex signal is mixed by a single-sideband upconverter with the 13.5-GHz signal generated by a coherent local oscillator (LO), as seen in Fig. 1. After filtering, the signal is sent to a power amplifier. A programmable attenuator in front of the power amplifier enables transmitting a power signal lower than its nominal value, so as to be able to assess the CFOSAT signal-to-noise ratio (SNR) conditions (CFOSAT SNR is ~6 dB per pulse instead of about 11 dB for KuROS in nominal conditions, see below). Then, the signal goes through a passive circulator. A mechanical switch in front of the antennas enables commuting between calibration channels and the LI or MI antenna channels, while a second switch on the MI antenna channel commutes between the H and V polarizations (see Fig. 1).

At the reception, the radar echo is multiplied by a chirp replica, whose highest frequency F_{repmax} cannot, however, exceed 180 MHz because of the limitation of the FPGA (Virtex-5 XC5VSX95T). We require that the beat signal between echo and replica is integrated over the whole pulse duration T_P and, as a consequence, the beat signal is analyzed only over the "analysis band" $B_A = F_{\text{repmax}} - F_{e\max}$. The range of distances sampled is $D = c(T_{\text{rep}} - T_P)/2$, where c is the velocity of light; and T_P and T_{rep} are the pulse and replica durations, respectively, whose values are chosen for each antenna depending upon altitude, as given in Table 2. All these modes are
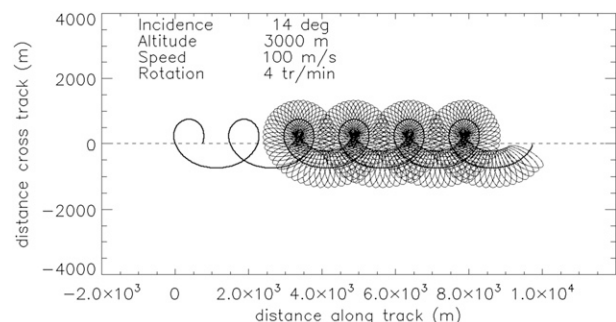

FIG. 3. LI antenna footprint along the aircraft track every 300 ms from altitude 3000 m, for a rate of 4 rpm, and an aircraft velocity of 100 m s^{-1}. The cycloid describing the trajectory of the footprint of the beam axis is also plotted.

TABLE 2. Radar parameters for the different modes of operation. Term H is the approximative flight altitude (above the surface), T_p is the pulse duration, and T_{rep} is the replica duration. Frequency range is the frequency band of the chirp generated by the transmitter. Term F_{repmax} is the highest frequency of the replica. Analysis band $B_A = F_{repmax} - F_{emax}$ is the frequency band after the deramping stage. Term N_{real} is the number of points after the decimation stage. Term N_{FFT} corresponds to the power of 2 number of points for FFT processing by extending the number of points by zero padding. SNR is given for one pulse, without integration.

Antenna	H (m)	PRI (μs)	T_p (μs)	T_{rep} (μs)	Frequency range $[F_{emin} - F_{emax}]$ (MHz)	F_{repmax} (MHz)	Analysis band B_A (MHz)	N_{real}	N_{FFT}	SNR (dB)
LI	3000	43.5	17	22.54	25–125	157.59	32.59	1352	2048	11.3
LI	2000	28.5	10.33	15.92	25–125	179.11	54.11	955	1024	16.6
LI	1000	16.5	5.66	8.56	25–125	176.24	51.24	514	512	25.6
LI	450	7.0	2	3.05	25–125	177.50	52.50	183	256	36.0
MI	3000	53.5	17	34.45	30–60	90.79	30.79	2067	2048	−5.4
MI	2000	37.0	10.33	24.48	30–60	101.09	41.09	1469	2048	−0.1
MI	1000	22.0	5.66	13.4	30–60	101.02	41.02	804	1024	8.9
MI	450	12.0	2	5.09	30–60	106.35	46.35	305	512	19.3

preloaded in the management and control unit and chosen by the operator during flights.

After going through the two switches and the circulator, the received chirps are sent to a low-noise amplifier. They are then filtered to limit the noise band and conserve only the upper band with the received signals. The microwave signal is down converted with the same coherent local oscillator as used in the transmitter part. The signals are then amplified, filtered by an antialiasing filter and sent to the analog-to-digital converter (ADC) of the DPU.

In nominal mode, the wave form is transmitted alternately at low rate (30 s) to the LI and MI antennas (for MI antenna, a switch commutes every 100 ms between the H and V polarizations). It is also possible to use continuously a single antenna (LI or MI antenna) or a single polarization for the MI antenna. All these modes are chosen by the operator during flight.

d. Digital processing unit

The digital processing unit is shown in detail in Fig. 5. After sampling the IF signal at 360 MHz, the first step of

the real-time onboard processing is the range compression. The raw signal is poorly resolved because of the long time impulse. Yet, as the transmitted signal is a chirp, a specific signal processing, called the deramping process (simple convolution by a replica signal) delivers the well-resolved signal.

The second step concerns the decimation stage. In Table 2, the analysis band, which corresponds to the maximum beat frequency resulting from the deramping processing, is 54 MHz at most. Therefore, a decimation factor of 6 is applied in order to reduce the complex sampling frequency from 360 to 60 MHz, and the low-pass filter was designed to cut off at 54 MHz.

The third step consists of an FFT processing providing the pulse response, corresponding to the backscattered power as a function of range.

The last step is the coherent integration of the complex samples over 1 ms for each range gate. We choose to use the pulse-pair processing technique (Zrnić 1977), which provides amplitude and phase of the mean signal with an efficient noise reduction. The maximum
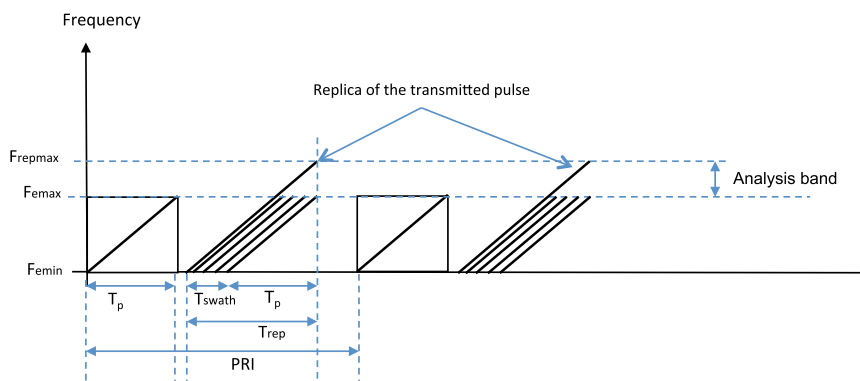

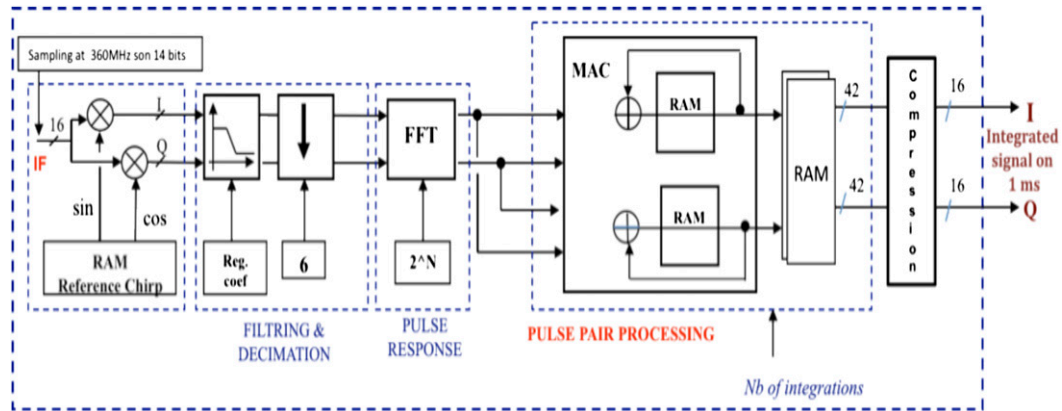FIG. 4. Time–frequency diagram of the transmitted pulses.

FIG. 5. Schematic diagram of the radar DPU.

amplitude of the Doppler velocity that can be measured (corresponding to a phase of the complex signal equal to π is $V_{D\max} = \lambda/(4\mathrm{PRI})$, where λ is radar wavelength and PRI is pulse repetition interval. From the values of PRI listed in Table 2, it follows that $V_{D\max}$ is at least equal to $103\,\mathrm{m\,s^{-1}}$, which is always larger than the line-of-sight velocity for the usual velocity of the plane ($\approx 100\,\mathrm{m\,s^{-1}}$).

The radiometric data [in-phase and quadrature (I&Q) signals integrated on 1 ms] and the ancillary data (aircraft attitudes, GPS time, . . .) are recorded at the same rate of 1 kHz.

e. Verification and calibration

Internal calibrations and measurements have been performed in a laboratory, involving an internal signal from a noise diode to check the stability of the receiver gain, and an internal 50Ω load to estimate the thermal noise level and to check the stability of the frequency and amplitude of the reflected signal on the load (transfer function restitution). The gain and losses of the complete chain have also been measured, and adequate corrections are deduced from these measurements and applied in ground postprocessing. Such tests involving a noise diode and a 50Ω load are also performed on board to check the stability of the instrument from flight to flight. A specific mode is used for this control (several chirp signals are transmitted and delayed, sweeping all the swath). The transmitted power is measured on board every second and stored in the data frame.

To assess the absolute level of the backscattered power, an external calibration was also performed using corner reflectors (trihedral reflectors) installed on an aircraft runway, overflown by the airplane during specific flights. Those measurements yielded a bias of $-0.2\,\mathrm{dB}$ when compared to the expected backscatter power levels (see section 4a below).

f. Expected performances on the estimation of the backscattering coefficient

The effective SNR_e, corresponding to the inverse of the radiometric resolution K_p, is given by the following relation (e.g., Ulaby et al. 1986):

$$\mathrm{SNR}_e = \frac{1}{K_p} = \frac{\sqrt{N_{\mathrm{int}}}}{\left(1 + \dfrac{1}{\mathrm{SNR}}\right)}, \qquad (1)$$

where N_{int} is the number of independent samples.

The error $\delta\sigma_o$ on the estimation of the backscattering coefficient (dB) is related to the radiometric resolution through

$$\delta\sigma_o = 10\log(1 + K_p). \qquad (2)$$

The signal is integrated coherently over 1 ms through onboard processing. The complex signal can then be integrated over a longer time by postprocessing. The objective is to estimate $\delta\sigma_o$ within a 0.2-dB maximum uncertainty. Table 3 presents the theoretical errors on the estimation of the backscattering coefficient depending on the SNR and the number of independent

TABLE 3. Theoretical errors on the estimation of the backscattering coefficient for the LI and MI antennas in the middle of antenna footprint for the 3000-m altitude modes of Table 2 (bold numbers). Term N_{PP} ($=T_I/\mathrm{PRI}$) is the number of integrated pulse pairs within the integration time T_I.

Coherent integration time T_I	1 PRI	1 ms	30 ms	100 ms
N_{PP} (LI antenna: PRI = 43.5 μs)	1	23	690	2300
SNR (dB) (LI antenna)	11.3	18.1	25.5	28.1
$\delta\sigma°$ (dB) (LI antenna)		**0.83**	**0.16**	**0.08**
N_{PP} (MI antenna: PRI = 53.5 μs)	1	18	540	1800
SNR (dB) (MI antenna)	−5.4	0.9	8.3	10.9
$\delta\sigma°$ (dB) (MI antenna)		**1.55**	**0.19**	**0.1**

FIG. 6. External view of both antennas aiming through the quartz windows.

samples. The results are calculated following different integration times for the two antennas for the 3000-m altitude mode. Those results show that it is necessary to integrate the signal over 30 ms, at least for both antennas to reach the objective of 0.2-dB estimation error.

g. Antenna performances

The antenna design was constrained by the use of a quartz window of 40-mm thickness, which was introduced to allow the whole radar system, including the antennas, to be within the aircraft body under cabin pressure. Efforts have been made through many numerical and laboratory tests to reduce the impact of this window on the antenna pattern. The Institut d'Electronique et de Télécommunications de Rennes (IETR) laboratory in charge of antenna design worked on the optimization of the weighting of each patch using the convex optimization method (Fuchs and Fuchs 2010) to get a main beam with the required specifications (aperture angles and direction). However, after installation on board, the first in-flight measurements on the corner reflectors in February 2012 revealed that for the MI antenna, the radiation pattern is significantly distorted. An external view of the antenna system mounted on the aircraft is shown in Fig. 6. The quartz window is supported by a circular metallic ring, seen in Fig. 6, and is at the origin of a diffraction effect, presumably responsible for this distortion. This drawback prevents us from obtaining reliable results in term of absolute σ° with the MI antenna, even though relative variations of σ° and Doppler measurements are not affected by this problem. Because of this antenna pattern distortion, the results from the MI antenna will not be presented in this paper.

In contrast, the radiation pattern of the LI antenna, whose field of view is nearer to the nadir direction, is not impacted by this metallic ring. This could be checked

from the calibration flights over corner reflectors, which yielded radiation patterns of the LI antenna very close to those obtained from laboratory tests, both in terms of shape and absolute level (bias -0.2 dB, rms difference 0.4 dB) as will be seen in section 4a below.

The advantages of this design with a beam pointing through a quartz window are the ease of instrument integration in the airplane, and the fact that the overall instrument is under aircraft pressure. However, the problem encountered with the MI antenna leads us to prepare an upgrading of the radar with a new design where this window will be removed. The modifications are presently under development.

3. Description of the campaigns

The first scientific use of KuROS occurred in March–April 2013 in the context of field campaigns carried out for two meteo-oceanographic programs. The first one is the Hydrological cycle in the Mediterranean Experiment (HyMeX; see Drobinski et al. 2014) in the northern part of Mediterranean Sea, while the second one is the Prévision Océanique, Turbidité, Ecoulements, Vagues et Sédimentologie (PROTEVS) project devoted to observation and modeling of currents, waves, and storm surge with a campaign in the Iroise Sea close to the Brittany coasts of France.

HyMeX is an international cooperative project organized with the aim of improving the understanding and quantification of the hydrological cycle and related processes in the Mediterranean, with emphasis on high-impact weather events. One of the scientific goals is to improve our understanding of intense sea–atmosphere interactions. To address this question, an experimental multiscale strategy has been designed with special observation periods (SOP) imbedded within enhanced observation periods and a long-term observation period. SOP 2 was organized in February–March 2013 in the northwestern part of the Mediterranean Sea to study intense air–sea exchanges and dense water formation. This region is exposed to regional offshore intense winds called mistral (northerly winds) and tramontane (northwesterly winds), usually associated with an anticyclonic system over the western part of France and a cyclonic system over the Gulf of Genova. These situations generate high sea state under fetch-limited conditions, and in winter and at the beginning of spring they also often generate oceanic convection. From 4 March to 15 April 2013, wind blew as mistral and/or tramontane for a total of more than 18 days in periods of 2–3 days of continuous strong (10–25 m s^{-1}) offshore winds. From 4 to 6 March, a cyclonic system located east of Spain generated strong easterly winds

$(10\text{–}20 \, \text{m s}^{-1})$ in the northern part of the Gulf of Lion basin.

During this SOP 2 experiment, in situ measurements (from ships, moored buoys, drifters) have been carried out. A meteo-oceanic buoy (called Lion buoy), moored in the Gulf of Lion (northwest of the Mediterranean Sea) provides surface parameters (10-m wind, directional spectra of surface gravity waves, air and sea temperature, atmospheric pressure) in an offshore region. Coastal buoys (Azur, Banyuls, Leucate, etc.) provide additional data of significant wave height, and mean wave period, and for some of them surface wind, and air and sea temperature.

During HyMeX, the French research aircraft ATR42 flight time was shared between two research teams and two types of measurements: in situ measurements in the boundary layer to provide mean and turbulent atmospheric quantities, and remote sensing measurements of the oceanic surface with KuROS. Because the optimal flight levels for KuROS are between 2000 and 3000 m, each flight period was divided in several subperiods, some of them dedicated to KuROS measurements with the 2000- and 3000-m flight levels. A total of 11 flights with KuROS data have been achieved during HyMeX. Table 4 gives the list of flights, the KuROS measurements during these flights, and the corresponding wind and wave conditions at the Lion buoy. An example of the flight plan during a tramontane event (northwesterly flight) is shown in Fig. 7.

The other field experiment during which KuROS was involved is PROTEVS. This experiment was designed and carried out by the French naval service Service Hydrographique et Océanographique de la Marine (SHOM). It is devoted to the study of wave–current interactions and storm surge conditions in the coastal region of Brittany. The goal is to improve the modeling of currents and waves with the Hybrid Coordinate Ocean Model (HYCOM, see http://hycom.org) and the wave model WAVEWATCH III (http://polar.ncep.noaa.gov/waves/index2.shtml), respectively. The area is characterized by very strong tide currents, complex bathymetry, coastal line, as well as frequent occurrence of long swell generated by Atlantic storms. Five Datawell directional waveriders were moored by SHOM in the area as well as several current sensors, which can also provide information on surface waves.

During this experiment, KuROS was flown over the area (see Fig. 8) with two flights on the same day (11 February 2013) separated by about 4 h. The first dataset (1111–1350 UTC) was collected after low tide (which occurred 1047 UTC), with the flight pattern of Fig. 8 described twice (once at 2000 and once at 3000-m altitude). The second dataset (1553–1659 UTC) was collected just before high tide (1650 UTC) with the flight pattern of Fig. 8 at 3000-m altitude. The situation of 11 February 2013 corresponds to a northwest swell with significant wave height of up to 6.8 m, a tide index of 107, and moderate wind ($\approx 6 \, \text{m s}^{-1}$).

4. Checks of the performance of the instrument from flight data

a. Calibration flights over corner reflectors

Five trihedral reflectors (40-cm edge, 32.5-dBm^2 radar cross section) were installed over a concrete surface, separated by about 50 m in the along-flight direction and 10 m in the across-track direction. Such a layout was chosen to spread the five reflectors over the KuROS footprint while flying at about 450 m above the surface. Several overpasses with KuROS have been carried out, with the KuROS antennas pointed either forward or backward with respect to the aircraft route. During the flight, in coordination with the radar operators on board the plane, ground operators adjust manually the tilt of the trihedral reflectors toward either 14° or 40° depending upon whether the LI or MI antenna is tested. This procedure enables us to assess the antenna radiation pattern and the absolute calibration.

Five overflights of the reflector system were performed during flight 12, but for one of them the flight track was not properly aligned with the system of reflectors, and for another one the aircraft altitude was varying during overflight, rendering the data difficult to interpret. Only the three remaining overflights were quite successful and were therefore retained for analysis. For each of those successful overflights, due to the 10-m across-track separation of the five reflectors, the reflector that is located closest to the flight track yields the highest power backscatter signature and only that one is retained for calibration analysis. The results are shown in Fig. 9. We also display the antenna radiation pattern obtained from the anechoic chamber measurements (blue line) and its Gaussian fit (red dashed line), with maxima coinciding with the 32.5-dBm^2 radar cross section of the trihedral reflectors at boresight. It may be seen that the retrieved shape and level of the antenna radiation pattern are remarkably consistent with the two-way radiation pattern obtained from laboratory tests. Over the 3-dB interval ($\approx 7°\text{–}20°$), the bias and rms difference between in-flight data and laboratory data are -0.2 and 0.4 dB, respectively. For incidence angles above $\approx 28°$, however, the lobe deviates radically from the Gaussian pattern because of the combined effects of secondary lobes, contribution of the ground to the backscattered power, and poor SNR.

TABLE 4. List of KuROS data during HyMeX campaign. The wave direction is calculated at the peak of the omnidirectional sea wave spectrum, from the triaxial instrument at the Lion buoy. When two values of wind and wave data are indicated, it means that we have considered two successive buoy measurements (1D spectra and directional data are obtained every hour and every 3 h, respectively). Both flights performed in Brittany refer to the PROTEVS campaign.

| Date	Flight No.	Time of KuROS acquisition at 2000- or 3000-m flight level (UTC)	Meteorological situation	Wind speed (m s^{-1})	Wind direction (°N)	Significant wave height (m)	Wave peak frequency (Hz)	Wave peak direction (from °N)
6 Feb 2013	4	1348–1742	Tramontane/mistral	13.4–13.9	280–290	2.5–3.1	0.135	310
11 Feb 2013	*6*	*1111–1350*	*Brittany–swell form northwest*			6.8	0.075	290
11 Feb 2013	*7*	*1553–1659*	*Brittany–swell form northwest*			6.8	0.075	290
13 Feb 2013	9	1325–1640	Tramontane/mistral	17.0	320–330	4.7–4.9	0.111	330
14 Feb 2013	10	0753–1300	Tramontane/mistral decreasing	10.8–11.8	340–350	2.4–2.7	0.146	360
15 Feb 2013	11	1033–1434	Tramontane/mistral	12.3–13.4	320–330	3.0–3.2	0.135	310
23 Feb 2013	13	1405–1436	Tramontane/mistral	17.5	320	5.4	0.0996	300
1 Mar 2013	14	1152–1432	Easterley wind conditions	14.9–15.4	70	4.5–4.9	0.111	90
2 Mar 2013	15	0613–0908	Tramontane/mistral decreasing	10.8–12.3	340–360	2.6–2.7	0.111–0.123	5–35
4 Mar 2013	16	1430–1815	Easterley wind conditions	9.8–10.3	120	1.4–1.5	0.193–0.217	100
5 Mar 2013	17	1245–1538	Easterley wind conditions	13.9–14.4	100	4.7	0.111	90–100
6 Mar 2013	18	1147–1422	Easterley wind conditions, 2 h after wind drop rotating	8.7–9.8	120	5.2–5.3	0.088	65
13 Mar 2013	20	1440–1803	Tramontane/mistral increasing period	16.4–18.0	320	3.3–4.0	0.111–0.123	310
14 Mar 2013	21	1355–1730	Tramontane/mistral	19.5	300	6.0–6.1	0.0996	310
15 Mar 2013	22	0713–1030	Tramontane/mistral	18.0–19.0	320	5.4–6.1	0.111	310–330
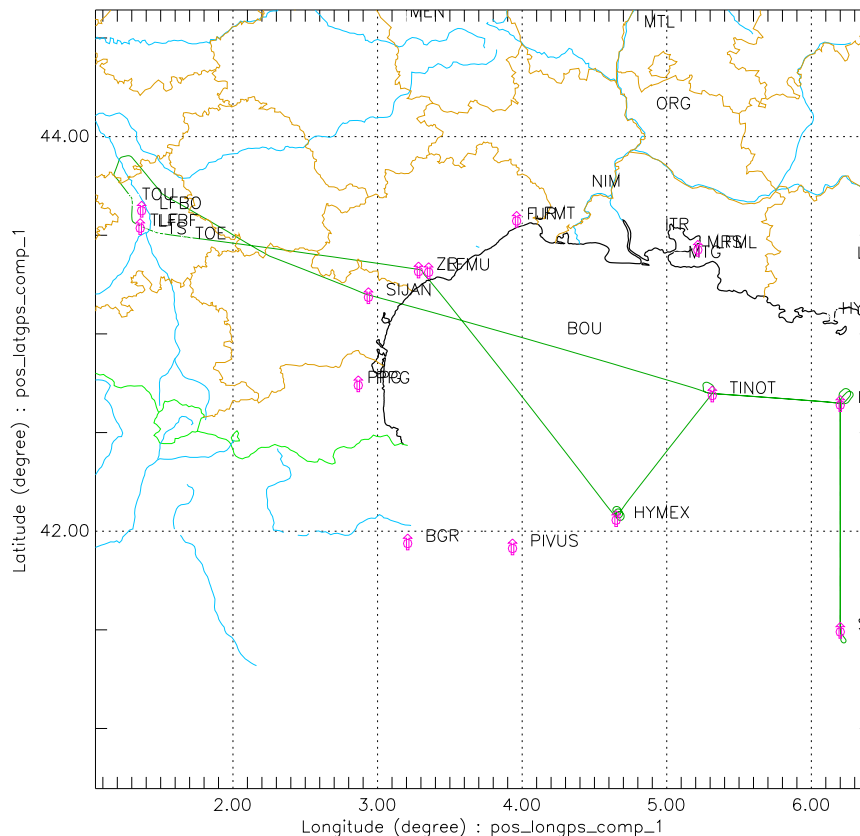
FIG. 7. Example of flight plan (green line) during SOP 2 of the HyMeX campaign (flight 18), provided by the SAFIRE team. The meteo-oceanic Lion buoy was moored at point labeled HyMeX.

The overflights over the trihedral reflectors can also be used to check the consistency of the Doppler velocity measured by the radar. This is illustrated in Fig. 10, where the Doppler velocity measured by the radar is compared with the line-of-sight velocity deduced from the aircraft inertial navigation system. Since the aircraft velocity is different from one overflight to the other, it would be meaningless to compare velocity measurements from different overflights, and therefore the data from only one overflight are displayed in Fig. 10, and only the data from the three most centered trihedrals (those yielding the highest power patterns) are shown. The quality of the retrieval of the Doppler velocity is virtually independent of the incidence angle between $7°$ and $20°$. Over that range of incidences, after averaging over the three overflights reported in Fig. 9, the average bias and rms difference for velocity are 0.4 and $0.5 \, \text{m s}^{-1}$, respectively. Below $6°$, because of the low altitude used for calibration flights ($\approx 500 \, \text{m}$), the uncertainty of the altitude retrieval limits the accuracy of the incidence angle assigned to each range gate, which explains the increased dispersion of the data. Above $\approx 31°$ incidence

angle, the SNR of the radar signal attains a threshold below which the Doppler velocity retrieval suddenly fails.

b. Assessment of the number of post-integrations to perform

We have seen in section 2d that the signal is integrated coherently over 1 ms by onboard processing, and that the complex signal can then be integrated over a longer time by postprocessing. Tests were performed with coherent and incoherent postprocessing with varying numbers of post-integrations. Figure 11 is an example of the power profile obtained over the sea from an altitude of 2000 m. The power profile integrated coherently over 1 ms is compared with the ones obtained by coherent and incoherent post-integration over 33 ms. Coherent post-integration over N samples should reduce the noise by $5 \log_{10} N$ (dB) while keeping the signal level unaffected. As expected, a comparison of the raw and coherently integrated data displayed in Fig. 11 follows this theoretical behavior. From various tests performed with different integration times, the post-integration time of
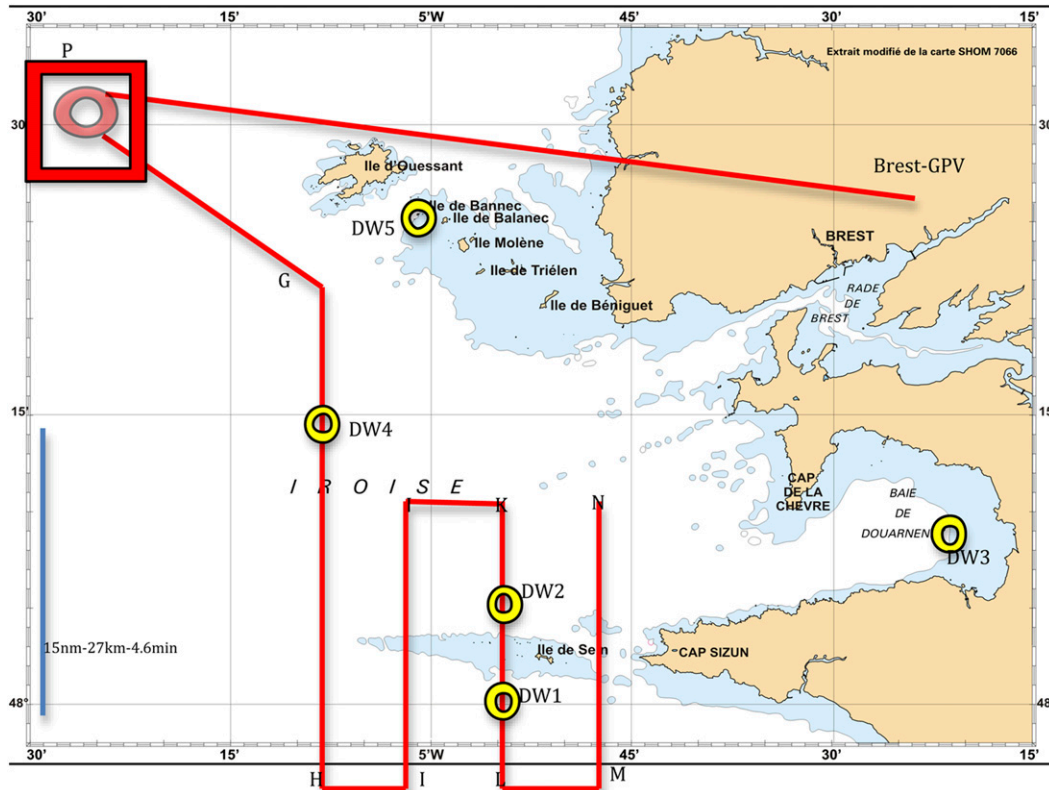
FIG. 8. ATR42 flight plan with KuROS during the PROTEVS campaign. The red pattern has been overflown 3 times (once at 2000 m around 1200 UTC, and twice at 3000-m flight level around 1300 and 1630 UTC).

33 ms was chosen for the results presented in this paper, providing a reasonable compromise between noise level and effective horizontal resolution (taking into account the displacement of resolution cells). In the worst case of a forward- or backward-viewing direction for an aircraft velocity of $100\,\mathrm{m\,s^{-1}}$, the footprint displacement during such an integration time is smaller than a range gate. As concerns the azimuthal shift, assuming, for example, a spin rate of the antenna of 4 rpm (equivalent to $24°\mathrm{s^{-1}}$), over the 33-ms post-integration time the antenna will rotate by $0.79°$ with respect to the vertical axis. For an incidence angle $\theta = 14°$, in the antenna frame this corresponds to an azimuth displacement of the antenna pattern by $0.79° \times \sin\theta = 0.19°$, which is no more than about 3% of the two-way azimuthal antenna beamwidth.

5. First results of $\sigma°$ and Doppler velocity

a. Analysis of the behavior of the $\sigma°$ signal

Figure 12 shows an example of the measured $\sigma°$ averaged over azimuth as a function of incidence angle. The absolute calibration of the data was obtained from laboratory measurements and assessed from the flights over corner reflectors by the method described in

section 4a. For this example the wind speed was $9\,\mathrm{m\,s^{-1}}$ and the significant wave height was $H_s \approx 5.3\,\mathrm{m}$. The standard deviation of $\sigma°$ over an incidence angle interval of $1°$ (indicated as error bars in Fig. 12) is on the order of ±1.5 to $\pm2\,\mathrm{dB}$, depending on incidence angle. This relatively high standard deviation is because $\sigma°$ is deeply modulated by the sea waves, and those modulations themselves will be used below to retrieve the sea wave spectrum. The average $\sigma°$ displayed in Fig. 12 may be compared to $\sigma°$ predicted by empirical geophysical model functions (GMF) that have been produced from satellite data. The GMF by Freilich and Vanhoff (2003) gives a modeled $\sigma°$ as a function of wind speed, and was built from observations of Tropical Rainfall Measuring Mission (TRMM) precipitation radar (PR) Ku-band radar for incidence angles between $0°$ and $18°$. This model function is based on the quasi-specular approach in the limit of Gaussian isotropic sea surface slope distribution, which is expected to be accurate for microwave scattering for $0° \leq \theta \leq 15°$. A quadratic multiparameter fit to TRMM PR data sorted according to wind and significant wave height was also performed over the incidence angle range from $5°$ to $18°$, from the large collocated database compiled by Tran et al. (2007), and
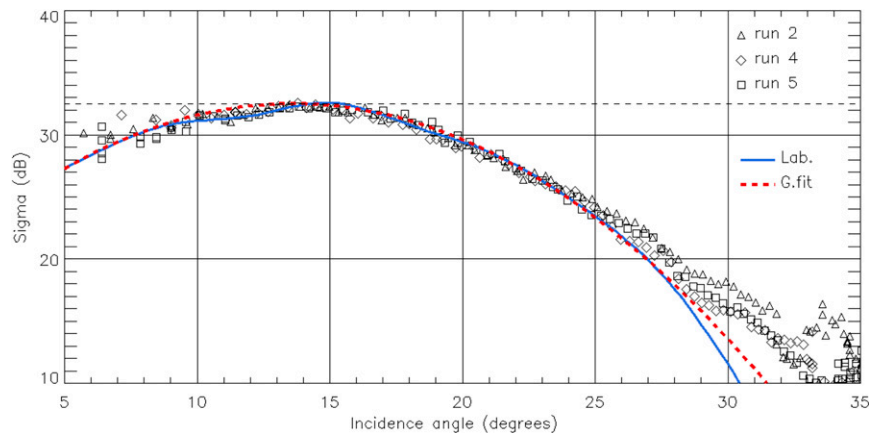
FIG. 9. Results from the LI antenna absolute calibration overflights on corner reflectors. Each symbol (triangle, diamond, square) corresponds to one of the three successful overflights. For each overflight, only the reflector located closest to the flight track (i.e., yielding the highest-power backscatter signature) is displayed. Antenna radiation pattern obtained from the anechoic chamber measurements (blue line) and its Gaussian fit (red dashed line), with maxima coinciding with the 32.5-dBm^2 radar cross section of the triedral reflectors at boresight.

the result for this wind and wave situation is also indicated in Fig. 12 as plus signs. Finally, the GMF by Wentz and Smith (1999) (thick solid line in Fig. 12) is based on the Ku-band National Aeronautics and Space Administration (NASA) scatterometer (NSCAT) data, which were available only for $\theta \geq 18°$. Our measurements are consistent with the TRMM models at low incidence angles, although it is ≈ 1 dB above the NSCAT model near $20°$ incidence. Such a difference is not significant given the difficulty to perform absolute intercalibrations of GMFs obtained from different satellites, as was shown by Caudal et al. (2005).

The azimuthal variation of $\sigma°$ can be easily studied because of the rotation of the antenna. Figure 13 shows

the azimuthal variation of $\sigma°$ for the case of flight 18 with an incidence angle of $20°$. The display includes 1 min of data, which corresponds to 2.4 rotations of the antenna. A least squares fit to the data is also displayed, involving five parameters (a constant and the phases and amplitudes of the two first harmonics). The azimuthal variation of $\sigma°$ from Wentz and Smith's (1999) GMF is also shown for comparison. Apart from the offset of average $\sigma°$ already identified in Fig. 12, the amplitude of the azimuthal modulation of the KuROS data fitted by two harmonics (± 1.1 dB) is fairly close to the amplitude obtained from Wentz and Smith's (1999) model (± 0.9 dB). For this example, the first maximum of the
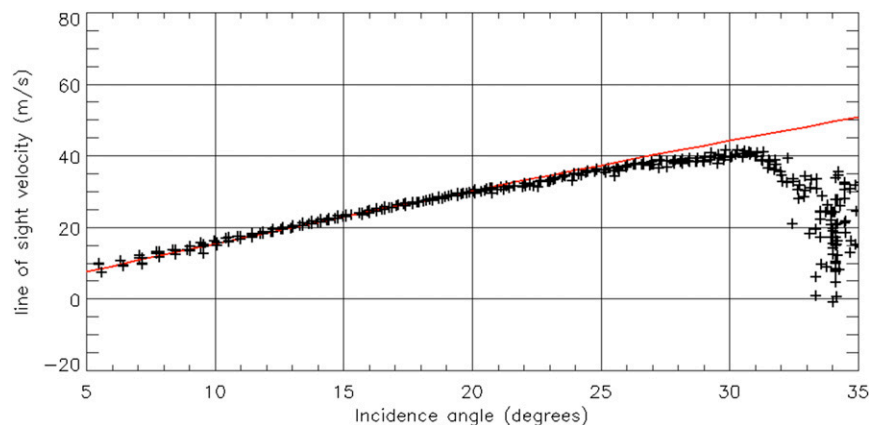

FIG. 10. Doppler velocity obtained by the radar from one overflight of the trihedral reflectors. Only data from the three most centered trihedrals (those yielding the highest-power patterns) are shown (plus signs). The red solid line is the theoretical radial velocity (proportional to $\sin\theta$) deduced from the aircraft INS.
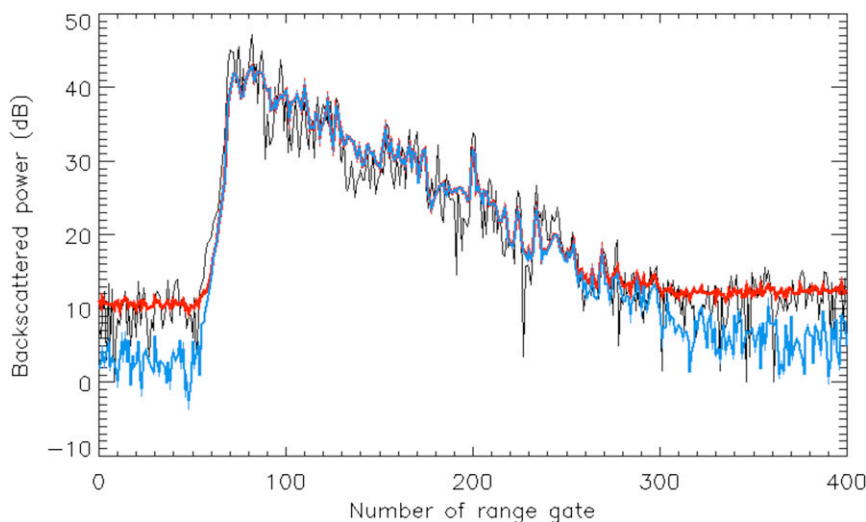
FIG. 11. Example of the radar power profile obtained over the sea at 2000-m altitude. Black line: coherent real-time integration over 1 ms, blue line: coherent post-integration over 33 ms, and red line: incoherent post-integration over 33 ms.

fitted curve occurs for an azimuth of 125°, which differs by no more than 5° from the average wind direction given by the buoy (≈120°). In Fig. 13 note the large variations (±4 dB) of the data around the fitted line. This is due to the small size of the elementary back-scattering surface in the range direction, which is determined by the pulse-limited range resolution of the radar (1.5 m), yielding an horizontal resolution of

≈6.2 m for a 14° incidence angle, which is much smaller than the typical wavelength of the dominant sea waves (a few hundred meters). The surface tilt variations due to those large-scale sea waves thus produce the deep modulations of $\sigma°$ observed in Fig. 13. Such modulations of $\sigma°$ can be used to measure sea wave directional spectra using the method described in section 5b below.
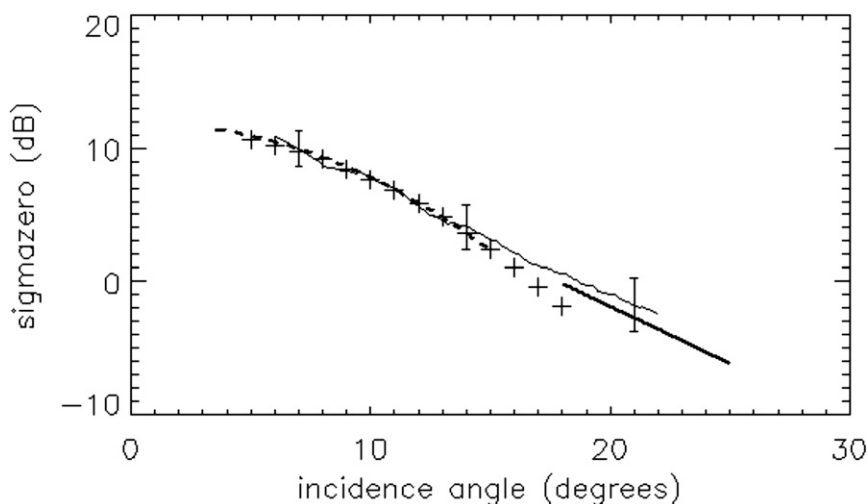

FIG. 12. Term $\sigma°$ averaged over the azimuthal directions as a function of incidence angle. The error bars indicate the standard deviation of the data over an incidence angle interval of 1°. Thin solid line: data obtained from KuROS on 6 Mar 2013 (flight 18, 1226:31 UTC) near the Lion buoy. The dashed line is Freilich and Vanhoff's (2003) model derived from TRMM precipitation radar data. Plus signs: quadratic fit to TRMM data involving U and H_s. Thick solid line: Wentz and Smith's (1999) model derived from NSCAT data. The wind speed is $U = 9\,\mathrm{m\,s}^{-1}$ and $H_s = 5.3\,\mathrm{m}$.

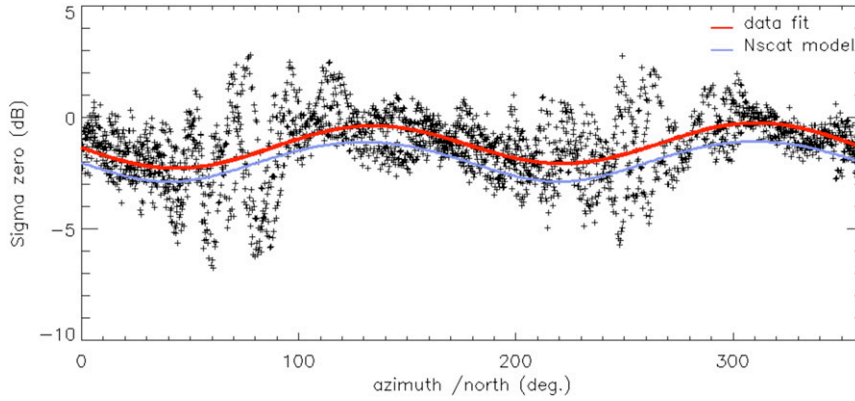FIG. 13. Term σ° as a function of azimuth, for an incidence $\theta = 20^\circ$, for the case shown in Fig. 12. Crosses: data obtained from KuROS. Red line: least squares fit to the data involving two harmonics. The large variation (± 4 dB) of the data around the fitted line is due to the presence of the long sea waves. Blue line: Wentz and Smith's (1999) empirical model derived from NSCAT data.

b. Measurement of the sea wave spectrum

The analysis of the modulations of radar reflectivity as a function of radial distance permits us to compute the directional sea wave spectrum along the direction of observation, while the rotation of the antenna around the vertical axis permits exploring all the azimuthal directions. The theory underlying this measurement technique was given by Jackson et al. (1985a) and is briefly reviewed here. For each azimuthal direction φ of the antenna, positions on the mean sea surface may be defined by their horizontal local coordinates x and y, where x is horizontal distance along the antenna-pointing direction, and y is along the azimuth direction. The elementary backscatter cross section σ is given by $\sigma = \sigma^\circ A$, where A is the area contained within a radar range gate. The presence of the large sea waves produces a tilt modulation of σ given as

$$\delta\sigma(x, y) = \sigma(x, y) - \overline{\sigma}(x, y), \qquad (3)$$

where $\overline{\sigma}(x, y)$ is the surface cross section that would occur if no large-scale wave were present.

The fractional modulation $m(x, \varphi)$ of the cross section seen by the radar is $\delta\sigma/\sigma$ averaged laterally across the beam:

$$m(x, \varphi) = \frac{\int G^2(y)(\delta\sigma/\sigma)\, dy}{\int G^2(y)\, dy}, \qquad (4)$$

where $G^2(y)$ is the two-way azimuth antenna radiation pattern.

In practice $m(x, \varphi)$ is obtained by removing a low-order polynomial fit from the measured radar power profile, thus eliminating the trend and retaining only the modulations.

The sea wave polar symmetric height spectrum $F(k, \varphi)$ is then obtained from the expression (Jackson et al. 1985a; Hauser and Caudal 1996)

$$F(k, \varphi) = \frac{L_y}{\sqrt{2\pi}\left(\cot\theta - \dfrac{\partial \ln\sigma_o}{\partial\theta}\right)^2} \frac{1}{k^2} P_m(k, \varphi). \quad (5)$$

In this expression, k, θ, and φ are the wavenumber, the incidence angle, and the azimuth, respectively. Term L_y is a length related to the azimuthal width of the beam footprint, and $P_m(k, \varphi)$ is the modulation spectrum, defined as

$$P_m(k, \varphi) = \mathrm{FT}[m(x, \varphi)] \times \mathrm{FT}^*[m(x, \varphi)], \qquad (6)$$

where FT refers to the Fourier transform operator, and the asterisk (*) stands for the complex conjugate.

As discussed by Jackson et al. (1985a), the speckle noise of the radar technique produces a supplementary modulation of σ°, which is included in the measured modulation spectrum, and this speckle noise must then be removed from the data for precise quantitative studies. To estimate the spectrum of the speckle noise, Hauser et al. (1992) used a semiempirical method based on the comparison between data integrated over different time intervals. Another approach was proposed by Engen and Johnsen (1995) in the context of the processing of SAR images. Those authors proposed to remove the speckle noise by computing image cross spectra between pairs of single-look SAR images separated in time. Following their approach, we replaced
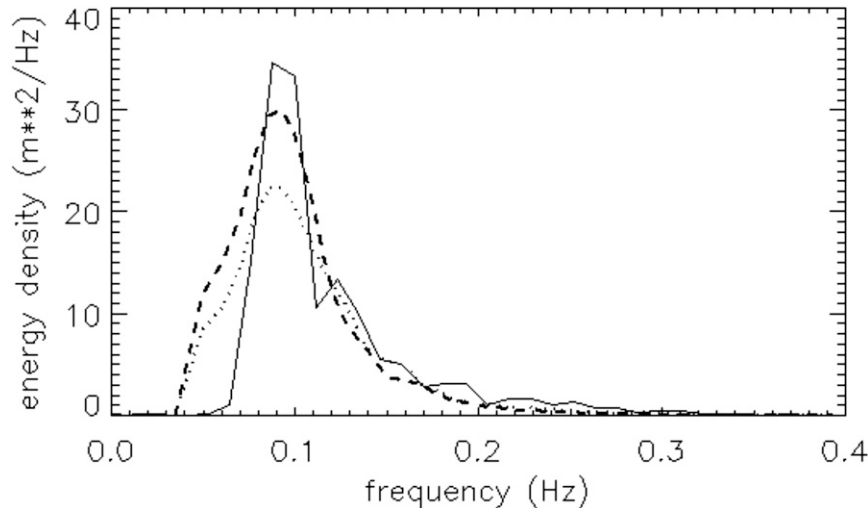
FIG. 14. Omnidirectional sea wave frequency spectrum from the Lion buoy at 1200 UTC 6 Mar 2013 (solid line). Omnidirectional frequency spectrum from KuROS just before overflight of the buoy (dotted line) and just after overflight (dashed line).

here the modulation spectrum $P_m(k, \varphi)$ from Eq. (6) above with the quantity

$$P'_m(k,\varphi) = \text{Real}\{\text{FT}[m(x,\varphi,t)] \times \text{FT}^*[m(x,\varphi,t+\delta t)]\}. \tag{7}$$

The time interval δt should be large enough that the speckle noise of both profiles is decorrelated but small enough that the radar footprint is only marginally displaced during that interval. Also, preliminary post-integration of the raw (1 kHz) data must be sufficient in order to provide a first reduction of the speckle. The interval δt is set to twice the post-integration time to ensure that the speckle noises of both profiles of Eq. (7) are well decorrelated. Here we requested a displacement of the footprint by less than 10% over the time interval δt. From 3000-m altitude with 4 rpm this implies that $\delta t \leq 80$ ms. Several trials were done with δt between 30 and 80 ms, which gave very similar results (the standard deviation of significant wave heights retrieved with those different assumptions was on the order of 3–5 cm for 2000-m flights as well as 3000-m flights). Since the post-integration time used routinely is 33 ms, in this paper we use $\delta t = 66$ ms.

Nevertheless, because of imperfect correlation between the sea wave signals at times t and $t + \delta t$, the computed $P'_m(k, \varphi)$ happens to be negative on some scarce occurrences. Since the sea wave spectrum should be a positive definite quantity, those values are artificially set to zero. This has virtually no effect on the retrieved significant wave height. The results obtained by this method are fairly consistent with speckle estimates

obtained using the approach of Hauser et al. (1992). The results presented below have been obtained by using this cross-spectral approach.

As an example, Fig. 14 shows a comparison between the omnidirectional sea wave spectrum measured by the Lion buoy and by KuROS (corrected from the speckle noise) for the flight of 6 March 2013. The hourly spectrum of the buoy is taken at 1200 UTC (the closest time to the overflight), and the KuROS spectrum just before and just after the overflight is shown. Although the sea wave field was rather inhomogeneous, the radar measurements are consistent with the hourly buoy measurement. The peak frequency observed by both KuROS and the buoy is ≈ 0.09 Hz. Significant wave height H_S is obtained by integrating the directional spectrum $F(k, \varphi)$ of Eq. (5) over the wavenumber space:

$$H_S = 4\sqrt{\int_{-\pi}^{\pi} \int_0^{\infty} F(k,\varphi)k \, dk \, d\varphi}. \tag{8}$$

The H_S measured by the buoy is 5.3 m, while the H_S from the radar is 5.1 and 5.6 m before and after the overflight, respectively.

Figure 15 shows an example of the sea wave directional slope spectrum $k^2 F(k, \varphi)$ measured by the radar. Such a spectrum was obtained from a dataset of 30 s, which corresponds to a little more than a rotation of the antenna in that case. Because of the 180° ambiguity of the slope spectrum analysis, only a symmetrized 2D spectrum is presented here. The question of the removal of this 180° ambiguity will be addressed in section 5c below.
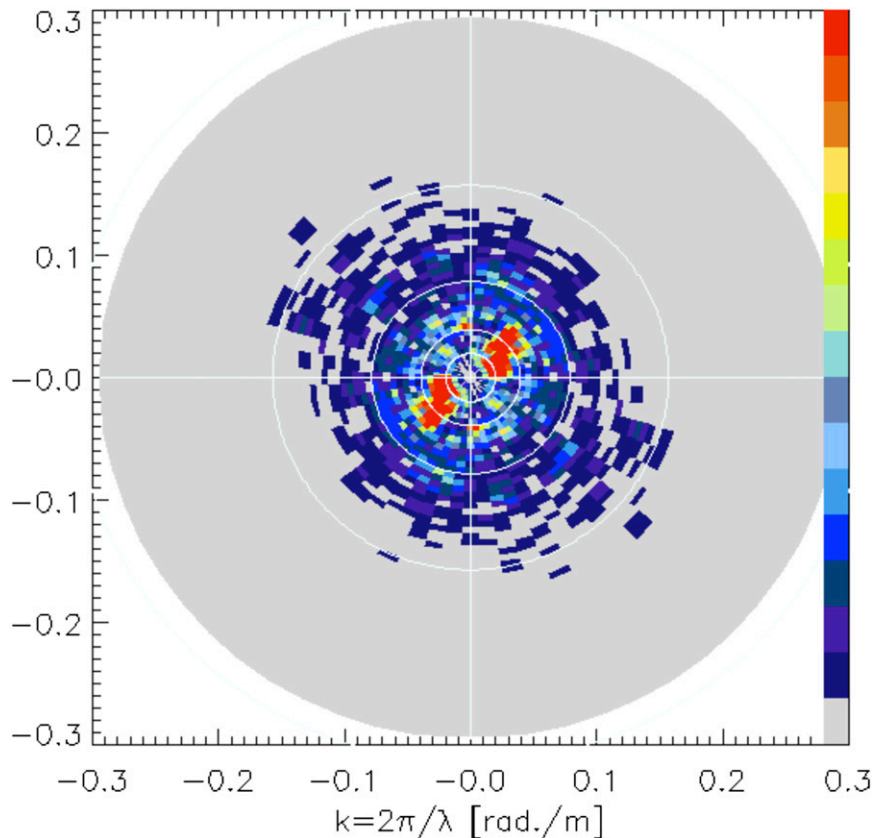
FIG. 15. Directional sea wave slope spectrum $k^2 F(k, \varphi)$ obtained from an altitude of 2000 m. Radial direction is wavenumber, and polar angle is azimuthal direction with north upward. The spectrum has been symmetrized because the measured modulation spectrum of $\sigma°$ is proportional to the sea wave slope spectrum. The color code corresponds to 16 identical intervals, from 0 to the highest value.

A more systematic comparison between KuROS and the sea wave buoy data during overflights has been performed in order to check the ability of KuROS to identify spectral peaks and to refine the calibration of the instrument in terms of H_S. The results, including the overflights performed during the HyMeX campaign, which are listed in Table 4, are shown as scatterplots in Fig. 16. As concerns the sea wave peak direction, the 180° ambiguity has been removed by reference to the buoy data. As indicated in Fig. 16, the correlation coefficient C between the buoy and radar measurements are particularly good for H_s ($C = 0.93$), and the correlation is somewhat weaker for both peak direction ($C = 0.81$) and peak frequency ($C = 0.81$). It may be noted that buoys provide sea wave spectra integrated over periods on the order of half an hour at one unique location, and thus the consistency between the wave parameters inferred from buoy and radar in Fig. 16 is quite satisfactory given the spatiotemporal inhomogeneity of the sea wave field. Overall, KuROS is remarkably efficient at identifying spatial inhomogeneities of the wave field occurring in limited fetch situations, which would not be attainable from a unique buoy.

c. Analysis using the Doppler signal

As the KuROS antenna is rotating around a vertical axis, the line-of sight velocity is alternatively positive or negative, depending upon the azimuthal orientation of the antenna. Typical velocities of the aircraft are on the order of 100 m s^{-1}, and thus for incidence angles smaller than 20° the Doppler velocity related to the aircraft motion ranges between -35 and $+35$ m s^{-1}. An example of the Doppler signal over the sea is shown in Fig. 17. The most important feature is the sinusoidal variation of the Doppler velocity as the antenna is rotating. From the analysis of measurements of Doppler velocities obtained with different orientations of the aircraft with respect to the wind and wave system, the average Doppler velocity signatures that we obtain are consistent with those expected from the aircraft motion,
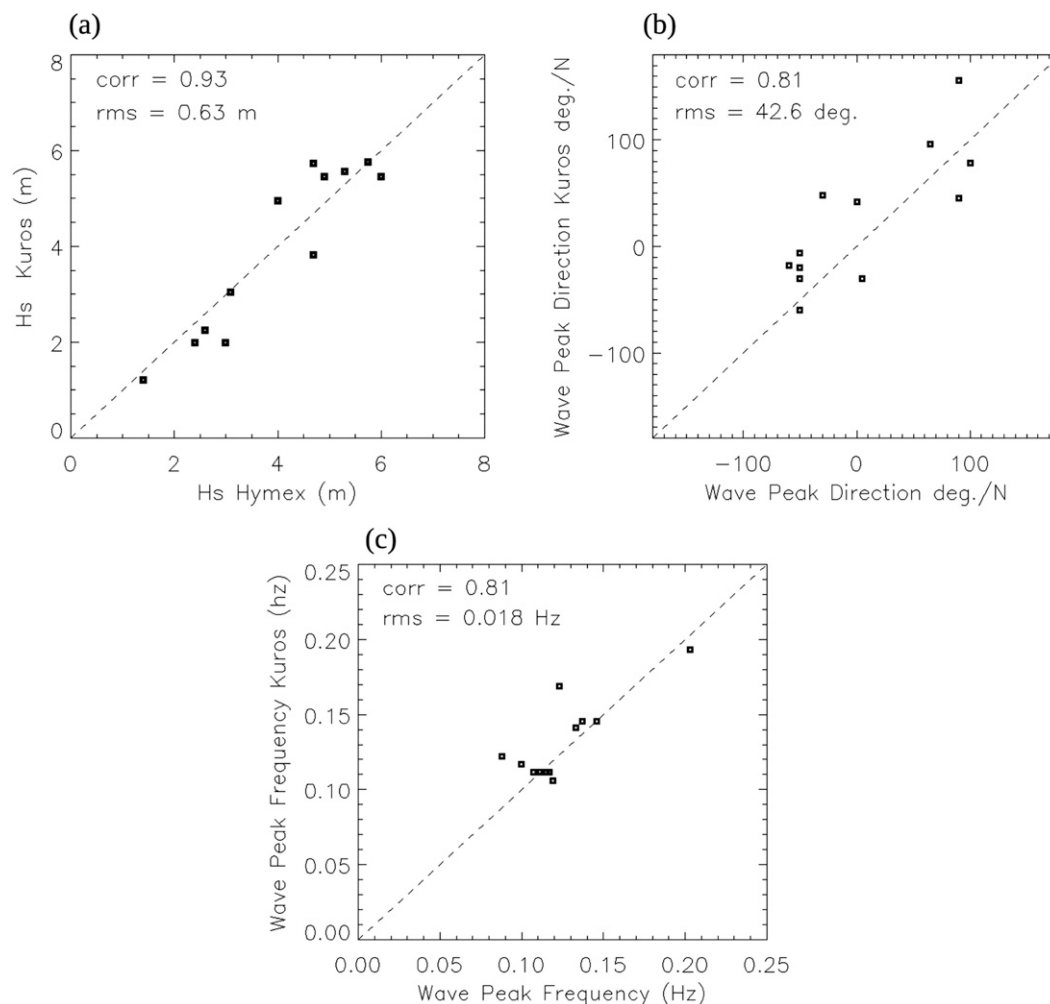
FIG. 16. Comparison between the observations performed by the Lion buoy (abscissa) and KuROS (ordinate) at the times of the overflights. The flights are those of the HyMeX campaign as listed in Table 4. (a) Term H_s, (b) wave peak direction, and (c) wave peak frequency. The correlation coefficient and rms difference between buoy and radar measurements are also indicated.

except that we needed to correct the antenna rotation angle by a systematic offset of 4°. This offset, presumably due to a misalignment of the antenna beam, has been systematically corrected from the data presented henceforth in this paper.

To study the velocity signature of the surface, this component related to the aircraft velocity has to be removed by using the ancillary velocity data given by the inertial navigation system (INS) of the plane. The residual Doppler shift or Doppler velocity anomaly, of interest here, is related to the kinematics of the sea surface. Note that the rms errors of the velocity components given by the INS are smaller than $3\,\mathrm{cm\,s^{-1}}$. Most of this error is related to the low rate of the INS data (25 Hz) while the KuROS data are recorded at a rate of 1 kHz. However, since only the spatial modulations of

velocities within each footprint will be used in this paper, those errors will have a negligible effect.

1) AMBIGUITY REMOVAL OF THE MEASURED SEA WAVE DIRECTIONAL SPECTRUM THROUGH THE ORBITAL VELOCITY OF SEA WAVES

Because of the changing orbital velocity along the phase of long surface waves, the front faces (as seen by the radar) of long waves propagating away from the radar have a positive line-of-sight velocity anomaly (orbital velocity directed away from the radar). The front faces of these waves are tilted toward the radar, so that the backscattered power is also greater. The modulations of the normalized radar cross section (NRCS) and Doppler velocity are therefore correlated. In contrast, in a situation of long waves propagating toward the
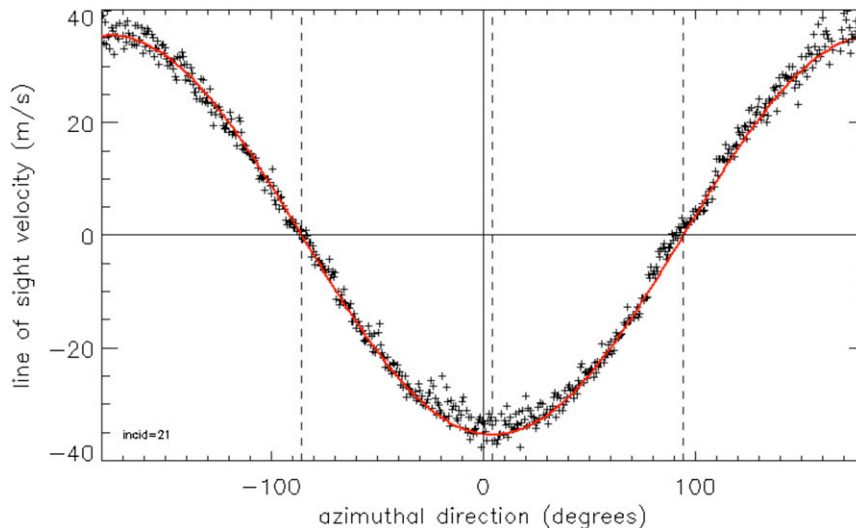
FIG. 17. Doppler velocity as a function of azimuthal direction of the antenna beam relative to the airplane velocity (including correction of airplane drift angle due to crosswind), for an incidence angle of 21°, measured over the sea from 3000-m altitude (plus signs). The vertical axis (solid line) is the direction along the aircraft velocity, while the vertical dashed lines are the directions along and perpendicular to the aircraft velocity, shifted by 4° due to antenna offset. The red solid line is the theoretical velocity expected from a motionless flat soil (taking into account the 4° antenna offset). The Doppler velocity is counted as positive for a displacement away from the radar.

radar, the Doppler anomaly signatures would be inverted and one would thus observe an anticorrelation between the NRCS and Doppler modulations. Thompson et al. (1991) obtained a clear signature of such a correlation between wave orbital velocities and the NRCS for Ku-band radar at an incidence angle of 20°.

Following this approach, we will assume that the orbital velocities dominate the wave-related velocity modulations. The correlations between the $\sigma°$ and velocity modulations are thus expected to be either positive or negative, depending upon whether the waves are traveling away from or toward the radar, respectively. The sign of this correlation can be obtained for each spectral component by computing the cross spectrum between the fluctuations of $\sigma°$ and velocity:

$$C_1(k, \varphi) = \mathrm{FT}\left[\frac{\delta\sigma_o}{\sigma_o}(x, \varphi)\right] \times \mathrm{FT}^*[\delta V(x, \varphi)], \quad (9)$$

where x is the horizontal distance along the direction of observation, FT is the Fourier transform operator along the x dimension, and the asterisk (*) denotes the complex conjugate. Terms $\delta\sigma°$ and δV are the $\sigma°$ and velocity modulations, respectively. To obtain them, one first removes the radial velocity due to airplane from the velocity signal (thus yielding the residual velocity). Then, one computes the smoothed radial profiles of $\sigma°$ and the

residual velocity, which are further removed to yield the modulations $\delta\sigma°$ and δV, respectively.

From the computed cross spectrum $C_1(k, \varphi)$, each sea wave Fourier component can be ascribed a propagation direction away from the radar if $\mathrm{Real}[C_1(k, \varphi)] > 0$, or toward the radar if $\mathrm{Real}[C_1(k, \varphi)] < 0$. Figure 18 displays the directional sea wave spectrum disambiguated by this method. It corresponds to the folded spectrum, which was given above in Fig. 15. The main wave train of Fig. 18 is seen clearly to be propagating toward the southwest. This is fully consistent with the direction of propagation of the sea waves as measured by the buoy, as will be shown below in section 5c(2).

2) COMPARISON WITH AMBIGUITY REMOVAL PERFORMED FROM THE PHASE VELOCITY OF SEA WAVES

It may be interesting to compare the method used above to remove the 180° ambiguity of the directional spectra to the approach that is used to retrieve ocean wave spectra from cross spectra of SAR images (Engen and Johnsen 1995). In the same manner as was done above in section 5b, the cross spectrum between two radar power profiles separated by some time lag ΔT can be computed, and the phase velocity of the sea wave can be deduced by analyzing its argument. The cross spectrum may be written as
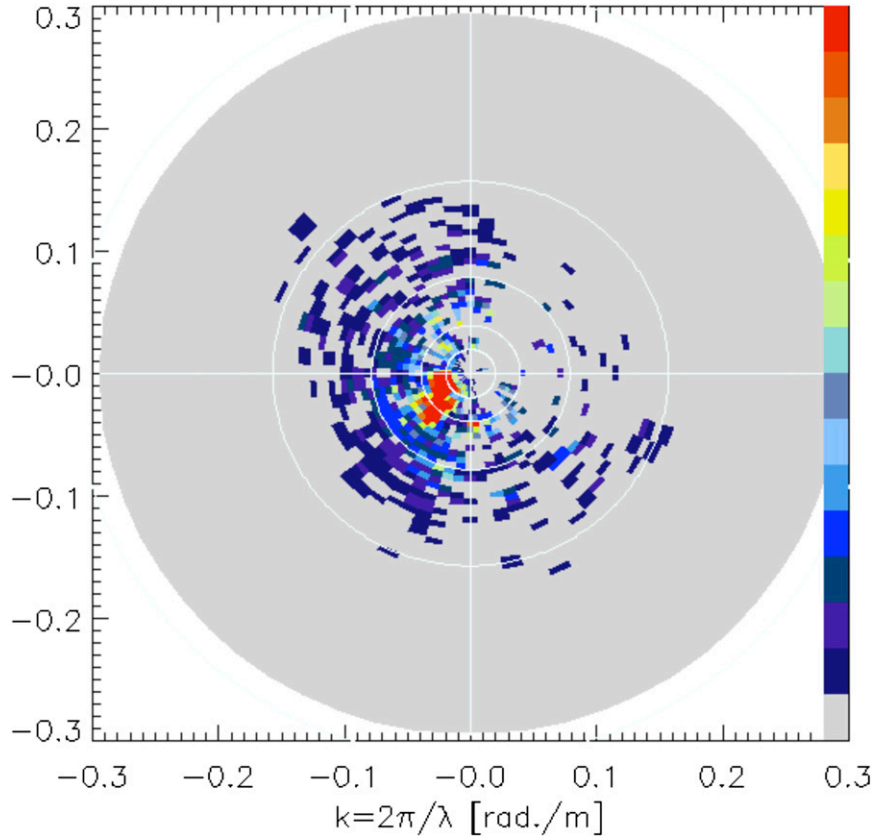
FIG. 18. As in Fig. 15, but the 180° ambiguity of the directional sea wave spectrum has been removed by combining the observations of $\sigma°$ and velocity (see text). North is upward, and the azimuth angle indicated is the direction toward which the sea wave component is propagating.

$$C_2(k, \varphi) = \text{FT}\left[\frac{\delta\sigma_o}{\sigma_o}(x, t)\right] \times \text{FT*}\left[\frac{\delta\sigma_o}{\sigma_o}(x, t + \Delta T)\right]. \quad (10)$$

For each wavenumber k, the phase velocity V_p of the sea wave propagating along the horizontal direction of observation may be obtained through

$$V_P(k, \varphi) = \frac{\delta p}{k\Delta T} - V_{\text{AH}}(\varphi), \quad (11)$$

where δp is the phase difference between the Fourier transforms of $\delta\sigma_o/\sigma_o$ at times t and $t + \Delta T$, and V_{AH} is the horizontal component of the aircraft velocity along the direction of observation. From Eq. (10) this may be rewritten as

$$V_P(k, \varphi) = \frac{1}{k\Delta T}\arctan\left\{\frac{\text{Im}[C_2(k, \varphi)]}{\text{Re}[C_2(k, \varphi)]}\right\} - V_{\text{AH}}(\varphi). \quad (12)$$

From the computed cross-spectrum $C_2(k, \varphi)$, each sea wave Fourier component can thus be ascribed a propagation direction away from the radar if $V_P(k, \varphi) > 0$, or

toward the radar if $V_P(k, \varphi) < 0$. This method thus permits to remove the direction ambiguity by merely comparing two snapshots of the surface obtained at times t and $t + \Delta t$, without the need to use the Doppler measurement.

The choice of the time lag ΔT is rather arbitrary. In section 5b [Eq. (7)], a short time lag of 66 ms was chosen in order to eliminate the speckle noise from two profiles containing virtually the same signal. Here instead we wish to identify the displacements of the wave trains; therefore, the time lag ΔT should be large enough that a significant phase shift is measured between times t and $t + \Delta T$, but small enough that the area illuminated by the radar is only marginally modified over that time interval. The illuminated area is moving under the combined effect of the aircraft velocity and antenna rotation. As a consequence the correlation between radial features obtained at times t and $t + \Delta T$ is imperfect, and therefore the cross spectrum $C_2(k, \varphi)$ of Eq. (10) is reduced, rendering the estimation of the sea wave phase velocity more noisy as ΔT is increased. Several trials were performed with different values of
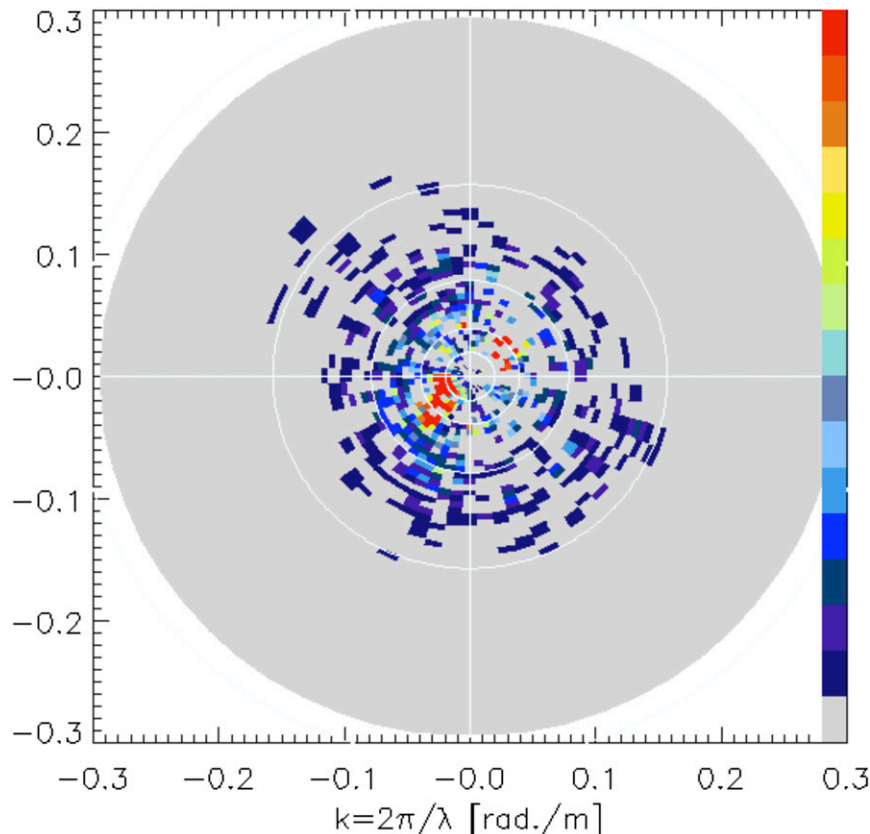
FIG. 19. As in Fig. 18, but the ambiguity removal is obtained from the phase velocity of sea waves instead of orbital velocity of the surface. The time lag is taken as $\Delta T = 0.4$ s.

ΔT, and the optimum was obtained for ΔT of a few tenths of a second, although the result is only weakly dependent upon the choice made for ΔT between 0.2 and 0.4 s. In this paper we take $\Delta T = 0.4$ s, which yields results that are the closest to the buoy data (see below).

Figure 19 displays the directional sea wave spectrum disambiguated by this method. It corresponds to the same case as Figs. 15 and 18. The overall direction is similar to the one retrieved from the orbital velocity (Fig. 18), with a main component propagating toward the southwest. However, the retrieved directions are more scattered, with an increased number of spectral components propagating along the opposite direction. The question is then whether the scarce components propagating toward the northeast in Fig. 19 are real features or an artifact due to the retrieving process.

To address this question, we compared both retrieved spectra of Figs. 18 and 19 with the ones deduced from the directional Lion buoy. For each wavenumber, however, the data from the directional buoy only consist of a power level and two complex harmonics, and a direct comparison with the much more detailed directional

spectra obtained from KuROS is therefore not relevant. We therefore computed the two first harmonics of the spectra obtained from KuROS, and then compared them directly to the buoy data. For each wavenumber, the directional spreading function of the sea wave spectrum may be written as

$$D(\varphi) = \frac{1}{2\pi}[1 + 2(a_1 \cos\varphi + b_1 \sin\varphi \\ + a_2 \cos2\varphi + b_2 \sin2\varphi)], \tag{13}$$

where φ is the azimuth, while a_1, b_1, a_2, and b_2 are real coefficients that are fitted to the data. The sets of coefficients (a_1,b_1) and (a_2,b_2) define the first and second complex harmonics, respectively. With respect to a rotation of 180°, the first harmonic is antisymmetric, while the second harmonic is symmetric, and thus the secondary component directed toward the northeast seen in Fig. 19 should correspond to a significant increase of the second harmonic. Validation of the ambiguity removal method will depend upon whether the buoy data show this increased second harmonic. To address this point, Fig. 20 displays the ratio $\rho = r_2/r_1$ between the
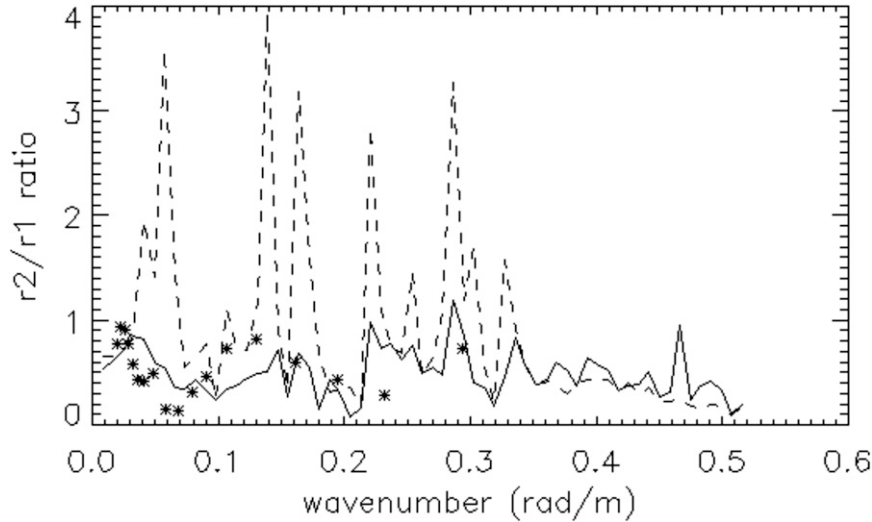
FIG. 20. Ratio $\rho = r_2/r_1$ between the second and first harmonics, as a function of wavenumber. Solid line: KuROS data disambiguated by the orbital velocity. Dashed line: KuROS data disambiguated by the phase velocity. Stars: buoy data.

amplitudes of the second and first harmonics, $r_1 = \sqrt{(a_1^2 + b_1^2)}$ and $r_2 = \sqrt{(a_2^2 + b_2^2)}$, respectively. For the set of wavenumbers sampled by the radar (from 0.02 to 0.3 rad m^{-1}), the ratio ρ deduced from orbital velocity (solid line in Fig. 20) exhibits moderate fluctuations, with an average of $\rho \approx 0.61$, which is close to the average ratio ρ obtained by the buoy ($\langle\rho\rangle \approx 0.55$). As a comparison, the ratio ρ deduced from the phase velocity in the optimal case ($\Delta T = 0.4$ s, dashed line in Fig. 20) is much more scattered, with a much larger average value ($\langle\rho\rangle \approx$ 1.14). This indicates that the secondary northeastern component appearing in Fig. 19 is not confirmed by the buoy data, whereas the spectrum of Fig. 18 is fairly consistent with the buoy data.

We performed such comparisons in a more systematic manner from overflights of the buoy performed on six different days with different wind and sea conditions. For each of those six cases, we computed the difference $\Delta\rho(k)$ between ratios ρ obtained by the radar and by the buoy at each wavenumber k from 0.02 to 0.3 rad m^{-1}. From this we deduced the rms average of $\Delta\rho(k)$ over k ($\langle\Delta\rho\rangle$). In all six cases studied, the method based on orbital velocity gave smaller $\langle\Delta\rho\rangle$ than the method based on phase velocity. The average value of $\langle\Delta\rho\rangle$ over the six overflights was found as 0.79 when the orbital velocity method was used, while it was as high as 1.61 when the phase velocity method was used.

The method based on orbital velocity (using the Doppler signature) thus appears to be more efficient at removing the 180° ambiguity on the sea wave directional

spectrum retrieved by KuROS, and should be preferred to the method using the phase velocity.

6. Conclusions

The new airborne Ku-band radar KuROS provides measurements of radial profiles of the normalized radar cross section $\sigma°$ over the sea surface at low and intermediate incidences. The antenna system is mounted on a platform rotating around a vertical axis in order to explore the different azimuthal directions. The spectrum of ocean waves with wavelengths larger than a few tens of meters is obtained by analyzing the modulations of the radial profiles of $\sigma°$. As the antenna is rotating, the different azimuthal directions are explored, allowing for retrieval of the directional spectrum of sea waves. In addition to measuring $\sigma°$, KuROS has the ability to measure the Doppler velocity of the radar echo, by means of the pulse-pair technique. This innovative implementation permits exploring the characteristics of the kinematics of the sea surface and removing the 180° ambiguity inherent to the principle of measurements based on the analysis of slope modulations of $\sigma°$ by a low-incidence real-aperture radar.

To address the question of measuring both wind and waves, the KuROS radar system includes two antennas, one probing a range of incidence angles around 14° [low incidence (LI) antenna] and another antenna probing incidence angles around 40° [medium incidence (MI) antenna]. However, the calibration flights over corner reflectors revealed a significant distortion of the radiation pattern of the MI antenna, presumably due to diffraction

by a metal collar used to adjust the antenna system within the body of the plane, and for this reason only the results from the LI antenna have been presented in this paper.

The KuROS radar has participated to two field experiments in 2013: the HyMeX program in the northern part of the Mediterranean Sea and the PROTEVS campaign in the Iroise Sea close to the Brittany coasts of France. We present the implication of KuROS within these field campaigns and give the first results from the observations performed during these campaigns.

Sea wave directional spectra computed from the radar observations during the HyMeX campaign were compared to the sea wave spectra produced by the Lion directional buoy moored in the Mediterranean basin. The speckle noise was removed from the data following the approach by Engen and Johnsen (1995), by computing the cross spectra between radar power profiles separated by some time lag δt taken as 66 ms. The data are consistent both in terms of significant wave height H_s and main features of the wavenumber spectrum. As concerns the azimuthal distribution, two methods were tested in order to remove the 180° ambiguity of the radar-derived directional spectrum. The first method consists of computing the cross spectrum between the modulations of $\sigma°$ and Doppler velocity, which permits removing the ambiguity by analyzing the sign of the correlation between the sea surface slope and the orbital velocity. The second method consists of computing the cross spectrum between the modulations of $\sigma°$ between two radar power profiles separated by some time lag ΔT, taken as a few tenths of a second. After removing the velocity of the aircraft, the phase of this cross spectrum permits deducing the phase velocity of sea waves in the terrestrial reference frame, whose sign yields the direction of propagation toward or away from the radar. The sea wave directional spectra disambiguated by both methods are then compared with the directional spectrum produced by the Lion buoy. From this analysis, we conclude that the method based on orbital velocity (using the Doppler signature) is more efficient at removing the 180° ambiguity on the sea wave directional spectrum retrieved by KuROS and should be preferred to the method using the phase velocity.

In the future we intend to use KuROS as a tool for geophysical studies involving the spatiotemporal evolution of the sea wave system in heterogeneous situations. In the context of the preparation of the future CFOSAT space mission, the cross-spectral method that we employed successfully to remove the speckle noise from the sea wave spectrum will permit us to study in more detail the behavior of the speckle noise in various wind and wave conditions, in order to be able to remove it with high accuracy from the satellite data. Other

studies will also be devoted to the estimate of the tilt velocity bias, which affects the Doppler signal (Chapron et al. 2005). Although the CFOSAT mission is not intended to have the Doppler measurement capability, the Doppler issues addressed in this paper with airborne radar will hopefully be useful in helping to define future satellite missions for observing the ocean surface.

REFERENCES

Caudal, G., E. Dinnat, and J. Boutin, 2005: Absolute calibration of radar altimeters: Consistency with electromagnetic modeling. *J. Atmos. Oceanic Technol.,* **22,** 771–781, doi:10.1175/JTECH1743.1.

Cavaleri, L., 2006: Wave modeling: Where to go in the future. *Bull. Amer. Meteor. Soc.,* **87,** 207–214, doi:10.1175/BAMS-87-2-207.

——, and Coauthors, 2007: Wave modelling—The state of the art. *Prog. Oceanogr.,* **75,** 603–674, doi:10.1016/j.pocean.2007.05.005.

Chapron, B., F. Collard, and F. Ardhuin, 2005: Direct measurements of ocean surface velocity from space: Interpretation and validation. *J. Geophys. Res.,* **110,** C07008, doi:10.1029/2004JC002809.

Drobinski, P., and Coauthors, 2014: HyMeX: A 10-year multidisciplinary program on the Mediterranean water cycle. *Bull. Amer. Meteor. Soc.,* doi:10.1175/BAMS-D-12-00242.1, in press.

Engen, G., and H. Johnsen, 1995: SAR-ocean wave inversion using image cross spectra. *IEEE Trans. Geosci. Remote Sens.,* **33,** 1047–1056, doi:10.1109/36.406690.

Freilich, M. H., and B. A. Vanhoff, 2003: The relationship between winds, surface roughness, and radar backscatter at low incidence angles from TRMM precipitation radar measurements. *J. Atmos. Oceanic Technol.,* **20,** 549–562, doi:10.1175/1520-0426(2003)20<549:TRBWSR>2.0.CO;2.

Fuchs, B., and J. J. Fuchs, 2010: Optimal narrow beam low sidelobe synthesis for arbitrary arrays. *IEEE Trans. Antennas Propag.,* **58,** 2130–2135, doi:10.1109/TAP.2010.2046863.

Gonzalez, F. I., and Coauthors, 1979: Seasat synthetic aperture radar: Ocean wave detection capabilities. *Science,* **204,** 1418–1421, doi:10.1126/science.204.4400.1418.

Hauser, D., and G. Caudal, 1996: Combined analysis of the radar cross-section modulation due to the long ocean waves around 14° and 34° incidence: Implication for the hydrodynamic modulation. *J. Geophys. Res.,* **101,** 25 833–25 846, doi:10.1029/96JC02124.

——, ——, G. J. Rijckenberg, D. Vidal-Madjar, G. Laurent, and P. Lancelin, 1992: RESSAC: A new airborne FM/CW radar ocean wave spectrometer. *IEEE Trans. Geosci. Remote Sens.,* **30,** 981–995, doi:10.1109/36.175333.

——, T. Podvin, M. Dechambre, R. Valentin, G. Caudal, and J.-F. Daloze, 2003: STORM: A new airborne polarimetric real-aperture radar for earth observations. *Proceedings of the Workshop on "POLinSAR": Applications of SAR Polarimetry and Polarimetric Interferometry,* H. Lacoste, Ed., ESA SP-529. [Available online at http://www.esa.int/esapub/conference/toc/tocSP529.pdf.]

——, C. Tison, J.-M. Lefèvre, J. Lambin, T. Amiot, L. Aouf, F. Collard, and P. Castillan, 2010: Measuring ocean waves from space: Objectives and characteristics of the China-France Oceanography Satellite (CFOSAT). *Ocean Engineering, Polar and Artctic Sciences and Technology,* Vol. 4, *Proceedings of the ASME: 29th International Conference on Ocean, Offshore and Arctic Engineering, 2010,* ASME, 85–90, doi:10.1115/OMAE2010-20184.

Jackson, F. C., W. T. Walton, and P. L. Baker, 1985a: Aircraft and satellite measurement of ocean wave directional spectra using scanning-beam microwave radars. *J. Geophys. Res.,* **90,** 987–1004, doi:10.1029/JC090iC01p00987.

——, ——, and C. Y. Peng, 1985b: A comparison of in situ and airborne radar observations of ocean wave directionality. *J. Geophys. Res.,* **90,** 1005–1018, doi:10.1029/JC090iC01p01005.

Pettersson, H., H. C. Graber, D. Hauser, C. Quentin, K. K. Kahma, W. M. Drennan, and M. A. Donelan, 2003: Directional wave measurements from three wave sensors during the FETCH experiment. *J. Geophys. Res.,* **108,** 8061, doi:10.1029/2001JC001164.

Plant, W. J., W. C. Keller, and K. Hayes, 2005: Simultaneous measurements of ocean winds and waves with an airborne coherent real aperture radar. *J. Atmos. Oceanic Technol.,* **22,** 832–846, doi:10.1175/JTECH1724.1.

Thompson, D. R., B. L. Gotwols, and W. C. Keller, 1991: A comparison of Ku-band Doppler measurements at 20° incidence with predictions from a time-dependent scattering model. *J. Geophys. Res.,* **96,** 4947–4955, doi:10.1029/90JC02210.

Tran, N., B. Chapron, and D. Vandemark, 2007: Effect of long waves on Ku-band ocean radar backscatter at low incidence angles using TRMM and altimeter data. *IEEE Geosci. Remote Sens. Lett.,* **4,** 542–546, doi:10.1109/LGRS.2007.896329.

Ulaby, F. T., R. K. Moore, and A. K. Fung, 1986: *Radar Remote Sensing and Surface Scattering and Emission Theory*. Vol. II, *Microwave Remote Sensing, Active and Passive*, Artech House, 608 pp.

Walsh, E. J., D. W. Hanckock, D. E. Hines, R. N. Swift, and J. F. Scott, 1985: Directional wave spectra measured with the surface contour radar. *J. Phys. Oceanogr.,* **15,** 566–592, doi:10.1175/1520-0485(1985)015<0566:DWSMWT>2.0.CO;2.

Wentz, F. J., and D. K. Smith, 1999: A model function for the ocean-normalized radar cross section at 14 GHz derived from NSCAT observations. *J. Geophys. Res.,* **104,** 11 499–11 514, doi:10.1029/98JC02148.

Zrnić, D. S., 1977: Spectral moment estimates from correlated pulse pairs. *IEEE Trans. Aerosp. Electron. Syst.,* **AES-13,** 344–354, doi:10.1109/TAES.1977.308467.